ENGINEERING Information Technology & Electronic Engineering
https://www.academax.com/EITEE; https://www.engineering.org.cn
https://ieeexplore.ieee.org/xpl/RecentIssue.jsp?punumber=11344065
E-mail: eng.itee@zju.edu.cn

Engineering Journals
Available on IEEE Xplore®

Research Article
https://doi.org/10.1631/ENG.ITEE.2026.0108

High-throughput estimation of aboveground peanut biomass with optimized spectral–textural features from unmanned aerial vehicle multispectral imagery

Liya HU[§1], Bo BAI[§2], Juntao YANG[1✉], Mingxuan SONG[1], Youwei LI[1], Dandan LIU[1], Zhenhai LI[1], Yirou LIU[2], Guowei LI[2✉]

[1]*College of Geodesy and Geomatics, Shandong University of Science and Technology, Qingdao 266590, China*
[2]*Institute of Crop Germplasm Resources, Shandong Academy of Agricultural Sciences, Jinan 250100, China*

Abstract: Accurate and efficient estimation of aboveground biomass (AGB) is important for peanut phenotyping and field management. This study evaluates spectral and textural features derived from unmanned aerial vehicle (UAV) multispectral imagery for nondestructive and high-throughput estimation of peanut AGB. Vegetation indices (VIs) and gray-level co-occurrence matrix (GLCM) texture features (TFs) are derived from the green, red, red-edge, and near-infrared bands and assessed via six regression models. The results reveal that near-infrared TFs exhibit the highest sensitivity to AGB. Among the GLCM configurations, a setting of a 7×7 window size, a 45° orientation, and 16 gray levels produces the most stable texture representation. Although combining all VIs and TFs slightly improves prediction accuracy, the relatively large differences between the coefficient of determination (R^2) and adjusted R^2 in some models suggest that the full feature set contains redundant predictors and has limited model parsimony. An extreme gradient boosting (XGBoost)–Shapley additive explanation (SHAP) feature selection strategy is therefore used to identify five key variables: difference vegetation index (DVI), variance, mean, energy, and modified soil-adjusted vegetation index (MSAVI). This compact feature set substantially reduces predictor dimensionality, limits the differences between R^2 and adjusted R^2 to below 0.020, and achieves consistent predictive accuracy, with R^2 above 0.840 and the root mean square error (RMSE) below 0.055 kg/m^2. The proposed approach provides a practical tool for high-throughput peanut biomass monitoring, phenotyping, and production management.

Key words: High-throughput monitoring; Unmanned aerial vehicle (UAV) remote sensing; Peanut; Aboveground biomass; Texture features (TFs)

1 Introduction

Peanut (*Arachis hypogaea* L.) is among the most important industrial oil crops worldwide and plays a crucial role in the supply of edible oil, food processing, and agricultural economies. In major peanut-producing countries, improving productivity and resource use efficiency has become increasingly important for meeting the growing demand for vegetable oil and supporting sustainable agricultural development (Bodoira et al., 2022). In this context, timely and accurate assessments of crop growth status are essential for both breeding programs and field-level production management (Hosseini Taheri et al., 2024). Among the various growth indicators, aboveground biomass (AGB) is a key variable reflecting canopy development, photosynthetic capacity, and dry matter accumulation, and is closely associated with yield potential and crop vigor. Reliable AGB information therefore provides an important basis for evaluating peanut growth performance and supporting management decisions in industrial crop production systems (He et al., 2021; Song et al., 2025).

Conventional AGB measurement relies on destructive sampling, which is labor-intensive, time-consuming, and impractical for large-scale or repeated monitoring throughout the growing season (Wang F et al., 2022). These limitations restrict its application in high-throughput phenotyping and routine field management of peanut (Zhang Y et al., 2021). Recent advances in unmanned aerial vehicle (UAV) remote sensing offer an efficient alternative by enabling rapid and nondestructive acquisition of high-resolution imagery over large areas (Cen et al., 2019). In particular, UAV-mounted multispectral sensors can capture canopy reflectance information related to plant physiological status and structural characteristics, making them well suited for field-based AGB estimation (Burns et al., 2022).

§ Equal contribution
✉ Juntao YANG, jtyang@sdust.edu.cn
Guowei LI, liguowei@sdnu.edu.cn
Liya HU, https://orcid.org/0009-0004-7145-9967
Bo BAI, https://orcid.org/0000-0001-9442-0433
Juntao YANG, https://orcid.org/0000-0002-7530-2623
Guowei LI, https://orcid.org/0000-0001-6128-8253
CLC number: TP79

Received: Apr. 17, 2026; Revision accepted: July 18, 2026; Crosschecked: Aug. 5, 2026

Numerous researchers have been committed to using remote sensing technology to estimate crop AGB in recent years, which can be generally divided into two categories: radiative transfer-based models and empirical statistical models (Yu et al., 2024). Radiative transfer-based models are usually based on the absorption and scattering between solar radiation and crop canopy, with a certain mechanism and strong versatility (Wang S et al., 2021; Franceschini et al., 2022). Nevertheless, radiative transfer-based models often incur high computational costs and require many input parameters, making it difficult to converge on the optimal solution (Kayad et al., 2022). In contrast, empirical statistical models are used to establish a relationship between AGB and vegetation indices (VIs), as VIs have been proven to effectively offer crop information about growth status through combination of two or more spectral bands. Thus, numerous methods have been developed for modeling the relationships between AGB and VIs, especially those based on red, near-infrared (NIR), or red-edge bands (Li and Potter, 2012).

However, owing to the low and spreading canopy architecture of peanut and the increasing saturation of spectral signals at later growth stages, biomass estimation based solely on spectral information remains challenging. This has motivated growing interest in integrating additional canopy structural information to improve the robustness and reliability of UAV-based peanut AGB estimation. Apart from spectral features, texture information can capture the inherent characteristics of crop canopy structures and provide complementary data correlated with crop growth parameters. To date, many studies have considered the combination of texture features (TFs) and VIs to accurately reflect the complex changes in crop canopy structure when the leaf area index (LAI), AGB, and nitrogen status are estimated (Zhang Y et al., 2021; Fan et al., 2023; Yang et al., 2023; Zhang SH et al., 2024). Previous work has revealed that the introduction of TFs into the model helps mitigate saturation issues and improves the accuracy of AGB estimation compared with the use of either the spectrum or texture alone, especially under high canopy density (Freitas et al., 2022; Liang et al., 2022).

Although numerous approaches have been proposed for crop AGB estimation and have achieved promising results (Xu L et al., 2022; Shu et al., 2023; Yue et al., 2023; Liu et al., 2024a), their applicability to peanut remains limited. Compared with cereals and tuber crops, such as wheat, maize, and potato, peanut plants exhibit a low-growing and laterally spread canopy and distinct physiological characteristics. These traits lead to different spectral responses and canopy structural patterns. As a result, the AGB estimation strategies developed for other crops cannot be directly transferred to peanuts. To date, only a limited number of studies have systematically evaluated the potential of UAV multispectral imagery for peanut AGB estimation, and the relationships between peanut AGB and VIs, TFs, or their combinations remain insufficiently understood. In addition, although TFs have been shown to enhance the estimation of LAI, AGB, and nutrient traits, most existing studies have relied on empirically selected single-band grayscale images and incorporated large numbers of TFs without systematic optimization (Zhang JY et al., 2021; Yang et al., 2023). The configuration of gray-level co-occurrence matrix (GLCM) parameters, including window size, orientation, and gray-level quantization, plays a critical role in determining the effectiveness of texture representation. However, comprehensive assessments of how these parameters jointly influence texture-based AGB estimation are still scarce. Previous studies have primarily adopted empirical parameter settings or examined individual parameters in isolation (Zheng et al., 2018; Liu et al., 2024a, 2024b). These approaches limit the robustness and transferability of texture-based models. These limitations highlight the need for a crop-oriented evaluation of spectral–textural feature configurations and a robust feature selection strategy tailored to peanut AGB estimation.

To address these issues, we develop a high-throughput estimation method for peanut AGB with optimized spectral–textural features using UAV multispectral imagery. Our key contributions are as follows:

1. A nondestructive and UAV multispectral imagery-based framework is proposed for high-throughput estimation of peanut AGB. By systematically evaluating VIs, TFs, and their combinations across multiple regression models, the proposed framework provides a practical solution for field-level AGB monitoring of peanut as a representative industrial oil crop.

2. Through a comprehensive assessment of spectral band sensitivity and GLCM parameter settings, the NIR-derived TFs are identified as the most informative for peanut AGB estimation, and an optimal configuration (a 7×7 window size, a 45° orientation, and 16 gray levels) is determined. These findings offer crop-oriented guidance for applying texture analysis to UAV-based AGB estimation.

3. To address feature redundancy and excessive dimensionality in the combined spectral–textural models, an extreme gradient boosting (XGBoost) model combined with Shapley additive explanation (SHAP) is employed to extract a compact set of key variables, namely, difference vegetation index (DVI), variance, mean, energy, and modified soil-adjusted vegetation index (MSAVI). The resulting low-dimensional feature subset improves model robustness and interpretability while maintaining high predictive accuracy, thereby enhancing the applicability of UAV-based AGB estimation in practical production and phenotyping scenarios.

2 Study site and materials

2.1 Brief description of the study area

The experimental region is located in Wangbian Community, Ningyang County, Tai’an City, Shandong Province, China, at a latitude of 35°50′N and a longitude of 116°39′E, with elevations ranging from 45 to 495 m, according to the General Bathymetric Chart of the Oceans (GEBCO) dataset (Fig. 1). It has a seasonally distinct climate with an average temperature of −2.1 ℃ in January and 26.8 ℃ in July. The lowest recorded temperature is −19 ℃, and the highest is 40.7 ℃. The annual sunshine duration is 2679.3 h, with a frost-free period of 199 days and an average annual precipitation of 689.6 mm.

2.2 Study materials

2.2.1 UAV multispectral imagery acquisition

UAV multispectral imagery was acquired using a DJI Mavic 3 Enterprise equipped with green, red, red-edge, and NIR bands. Flights were conducted between 10:00 and 14:00 on June 7, June 12, July 5,

Fig. 1 Experimental field and sampling locations

and July 20, 2023, under clear-sky conditions. The main specifications of the UAV platform and multispectral sensor are summarized in Tables 1 and 2. Raw images were processed in DJI Terra for lens-distortion correction, global navigation satellite system (GNSS)/inertial measurement unit (IMU)-based geometric alignment, band-to-band registration, radiometric calibration using reflectance panels, and orthomosaic generation. The resulting orthomosaics were georeferenced in ArcMap (ArcGIS 10. X) using the D_Xian_1980 geodetic datum and projected to the Xian_1980_GK_Zone_18 coordinate system.

Table 1 Spectral parameters of the multispectral sensor

Parameter	Value			
	Green	Red	Red-edge	NIR
Center wavelength (nm)	550	660	735	790
Bandwidth (nm)	40	40	10	40
Wavelength range (nm)	530–570	640–680	730–740	770–810

Table 2 UAV system parameters

Parameter	Value
Time of endurance (min)	45
Flight altitude (m)	20
Image resolution (pixels)	640×512

2.2.2 Field data collection of peanut AGB

The experimental materials were sown on May 12, 2023, with field observations conducted from May 22 to July 20, and the harvest was completed on September 23, resulting in a growth period of approximately 134 days. To improve soil hydrothermal conditions and ensure uniform seedling establishment, ridging and plastic film mulching were applied across the experimental field. All treatments followed a unified fertilization regime, with application rates equivalent to 0.024 kg/m^2 of pure nitrogen and 0.024 kg/m^2 of potassium dihydrogen phosphate. Except for the prescribed fertilization and cultivation practices, all other field management operations were conducted under identical standardized conditions to minimize external variability and ensure data comparability.

The experimental field was divided into 43 plots, each corresponding to a distinct peanut germplasm resource. All plots were arranged in double rows on each ridge, with single-seed sowing and a uniform plant spacing of 15 cm. Destructive sampling of AGB was conducted at four key growth stages: the seedling stage (June 7), flowering–pod initiation stage (June 12), pod development stage (July 5), and pod maturation stage (July 20). At each sampling event, six representative plants were randomly selected from each plot. Roots were removed, and the aboveground portions were cleaned, oven-dried at a constant temperature to a stable weight, and weighed individually. The dry weights of the six plants from each plot were summed to obtain plot-level biomass, which was subsequently converted to AGB per unit area (kg/m^2) based on the planting density of each plot.

A total of 43 plots were investigated in this study, and AGB measurements were collected at four growth stages, resulting in 172 samples (43 plots×4 stages). The descriptive statistics of the measured AGB across the four stages are summarized in Table 3. The data show a clear increasing trend in both mean values and variability (standard deviation) as the peanut plants progressed through the growth stages, indicating successful capture of the dynamic biomass accumulation process.

To ensure the independence of the training and validation datasets, a plot-level splitting strategy was adopted. Specifically, data from plots 1–30 (30 plots×4 stages, 120 samples) were used as the training set, while data from plots 31–43 (13 plots×4 stages, 52 samples) were used as the validation set.

Table 3 Descriptive statistics of field-measured AGB across different growth stages

Date	Field-measured AGB (kg/m^2)			
	Min	Max	Mean	Standard deviation
June 7	0.0067	0.0211	0.0130	0.0032
June 12	0.0325	0.0866	0.0526	0.0116
July 5	0.0729	0.3306	0.1476	0.0482
July 20	0.1413	0.6017	0.3933	0.0865

3 Methodology

To support practical and high-throughput estimation of peanut AGB under field conditions, this work proposes an application-oriented methodological framework based on UAV multispectral imagery. The overall workflow (Fig. 2) consists of UAV data acquisition and preprocessing, extraction of spectral and textural features, systematic evaluation of texture parameter configurations, feature optimization, and construction of regression models for AGB estimation.

3.1 Calculation of the vegetation indices

Spectral information, particularly vegetation indices derived from canopy reflectance, provides a nondestructive means of assessing crop photosynthetic capacity and growth status (Qiao et al., 2022). From the UAV multispectral imagery, 10 commonly used VIs are calculated, including normalized difference vegetation index (NDVI), normalized difference water index (NDWI), green normalized difference vegetation index (GNDVI), soil-adjusted vegetation index (SAVI), normalized difference red-edge index (NDRE), ratio vegetation index (RVI), near-infrared reflectance

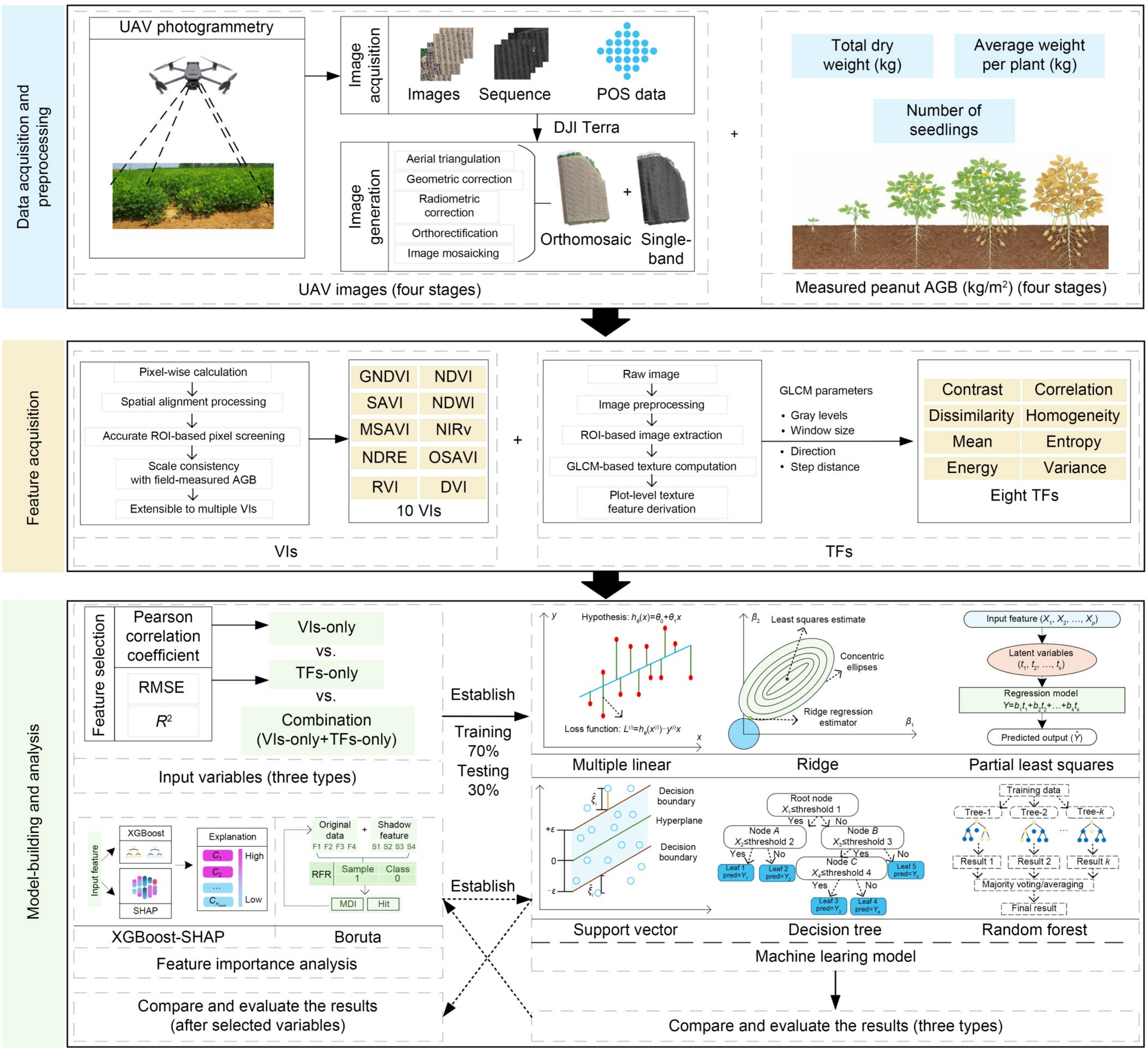

Fig. 2 Workflow of this work. θ denotes the model parameters in the hypothesis function with θ_0 being the intercept and θ_1 being the regression coefficient. i in $\hat{\xi}_i$ is the sample index (i=1, 2, $\cdots$, n). n_{SHAP} denotes the number of SHAP feature contributions. C denotes the contribution of SHAP. POS denotes position and orientation system. MDI denotes mean decrease in impurity

of vegetation (NIRv), MSAVI, DVI, and optimized soil-adjusted vegetation index (OSAVI). Their formulas are provided in Table S1 in the supplementary materials.

All VIs are calculated at the pixel level. To ensure spatial consistency among the input bands, the red, green, and NIR images are resampled using bilinear interpolation to match the spatial resolution of the red-edge band. The resulting VI maps are generated for the entire study area and stored in the tagged image file format (TIFF).

To derive plot-level VI values corresponding to the field-measured AGB and TFs, region-of-interest (ROI) boundaries are used to extract valid pixels from each experimental plot. The geographic coordinates of the plot boundaries are converted into image row and column indices using the raster geotransformation parameters. The Shapely library is then used to construct polygon geometries for the plot boundaries. Valid pixels are identified by traversing the bounding rectangle of each polygon and determining whether the corresponding pixel centers are located within the polygon. The mean value of all valid pixels within each ROI is calculated as the plot-level VI value. Representative VI distributions across the four growth stages are shown in Fig. S1 in the supplementary materials.

3.2 Calculation of the texture features

TFs describe the spatial homogeneity and structural organization of vegetation and provide complementary information to spectral features (Chen et al., 2021; Balling et al., 2023). In this study, TFs are extracted using GLCM to characterize the spatial heterogeneity of the peanut canopy (Niu et al., 2025). The green, red, red-edge, and NIR bands are independently evaluated.

Before GLCM construction, each single-band image is normalized to an 8-bit grayscale range and quantized into 16, 32, and 64 gray levels. GLCMs are calculated using window sizes of 3×3, 5×5, and 7×7, a pixel offset of 1, and orientations of 0°, 45°, 90°, and 135°. Eight GLCM metrics—mean, variance, homogeneity, contrast, dissimilarity, entropy, energy, and correlation—are extracted, and their definitions are provided in Table S2 in the supplementary materials.

A total of 1152 TFs are generated from four spectral bands, three window sizes, four orientations, three gray-level settings, and eight texture metrics. Plot-level TF values are obtained by averaging valid pixels within the corresponding ROI masks. Border-replication padding is applied before sliding-window calculation to reduce edge effects. Representative TF distributions are shown in Fig. S2 in the supplementary materials.

3.3 Selection of the optimal feature variable

Pearson correlation analysis is used to assess the relationships between candidate features and measured AGB (Schober et al., 2018). Boruta and XGBoost-SHAP are then applied as two feature selection strategies to reduce feature redundancy and identify informative variables. Boruta uses a random forest regressor to retain variables whose importance consistently exceeds that of randomly generated shadow features (Kursa and Rudnicki, 2010). For XGBoost-SHAP, the XGBoost model is optimized using five-fold cross-validation, and Tree-SHAP is used to quantify feature contributions (Nohara et al., 2022).

3.4 Construction of the regression model

For peanut AGB estimation, six representative regression models are evaluated, including three linear models—multiple linear regression (MLR), ridge regression (RR), and partial least squares regression (PLSR)—and three nonlinear models—support vector regression (SVR), decision tree regression (DTR), and random forest regression (RFR). These models are selected to compare the performance of interpretable linear approaches with that of nonlinear methods which can capture complex relationships between canopy features and AGB (Burnett et al., 2021; Hou et al., 2025).

3.5 Assessment of the model performance

The coefficient of determination (R^2) is used to evaluate the goodness of fit of the six AGB estimation models, with higher values indicating stronger agreement between the observed and predicted AGB. To account for differences in model complexity and avoid overestimation of explanatory power caused by redundant variables, the adjusted R^2 (R^2_{adjusted}) is also calculated, which penalizes the inclusion of unnecessary predictors. In addition, the root mean square error (RMSE) is employed to quantify the prediction accuracy, with lower values indicating better model performance. These evaluation metrics are defined as follows:

$$R^2 = 1 - \frac{\sum_{i=1}^{n}(f_i - y_i)^2}{\sum_{i=1}^{n}(y_i - \bar{y})^2}, \tag{1}$$

$$R^2_{\text{adjusted}} = 1 - (1 - R^2)\,\frac{n-1}{n-k-1}, \tag{2}$$

$$\text{RMSE} = \sqrt{\frac{1}{n}\sum_{i=1}^{n}(f_i - y_i)^2}, \tag{3}$$

where f_i denotes the i^{th} predicted value, y_i represents the i^{th} observed value, $\bar{y}$ indicates the mean of all the observed values, n is the sample size, and k is the number of independent variables.

4 Experimental result analysis

4.1 Correlation analysis of vegetation indices

To evaluate the applicability of VIs for AGB estimation, Pearson correlation analysis is conducted between the 10 VIs and measured AGB. Fig. 3 presents the corresponding scatterplot matrices. In each scatterplot matrix, the diagonal panels show the marginal distributions of individual variables using blue histograms and density curves, whereas the off-diagonal panels show the pairwise relationships among the variables. In the off-diagonal panels, the orientation of the blue scatter patterns and red ellipses indicates the direction of the correlation, whereas narrower ellipses represent stronger linear relationships.

The diagonal distributions show that GNDVI (Fig. 3a) and NDWI (Fig. 3b) are approximately symmetric with slight skewness, whereas DVI and MSAVI exhibit right-skewed distributions, with observations concentrated mainly in the lower-value ranges (Fig. 3a). Except for NDWI, most VIs are significantly positively correlated

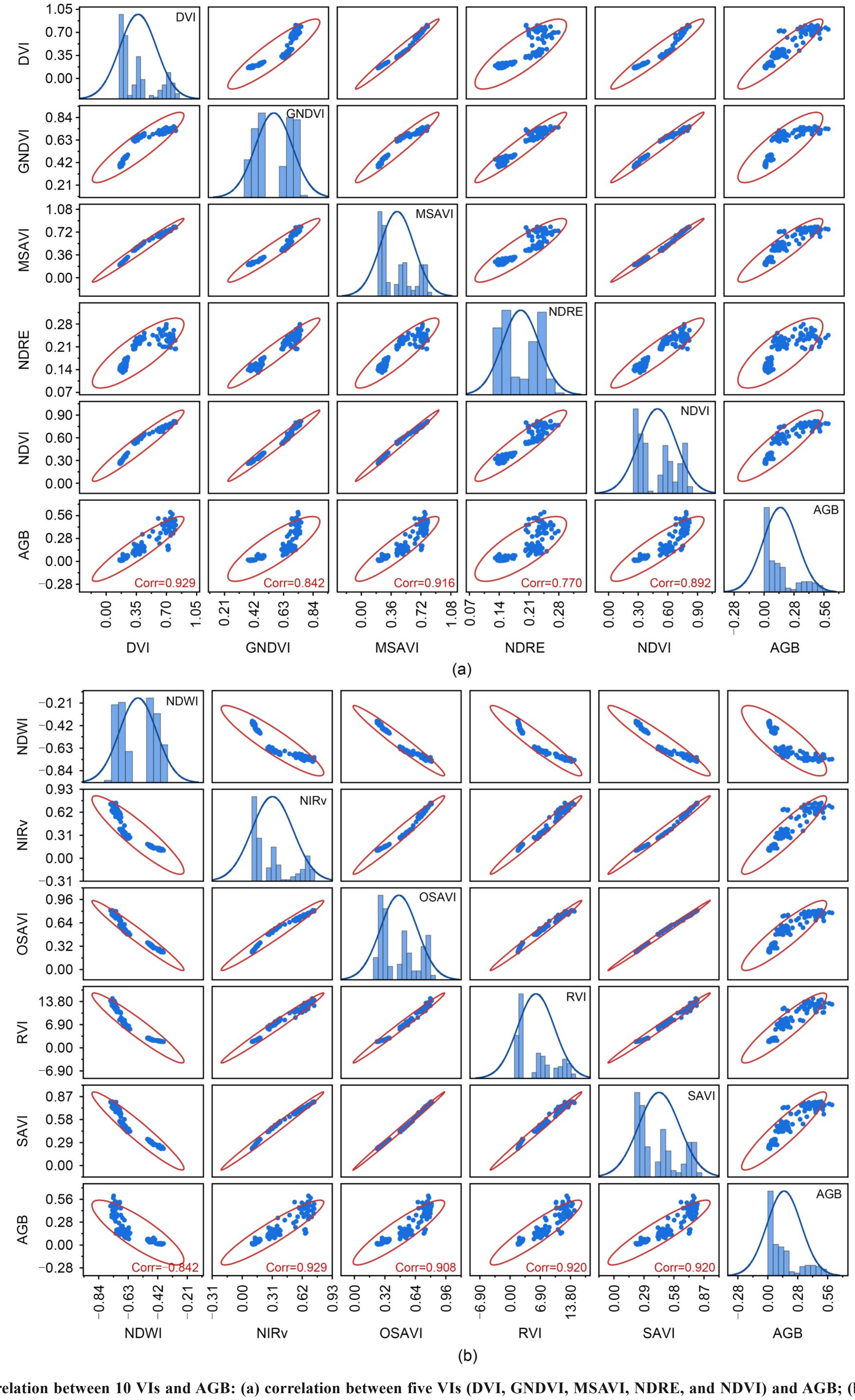

Fig. 3 Correlation between 10 VIs and AGB: (a) correlation between five VIs (DVI, GNDVI, MSAVI, NDRE, and NDVI) and AGB; (b) correlation between five VIs (NDWI, NIRv, OSAVI, RVI, and SAVI) and AGB. Corr denotes the correlation

with peanut AGB. In particular, DVI and NIRv exhibit the strongest positive linear relationships with AGB, as indicated by their concentrated scatter distributions and narrow correlation ellipses. In contrast, NDWI is negatively correlated with AGB, reflecting a spectral response more closely associated with canopy water status than with biomass accumulation. Based on this inverse relationship, NDWI is excluded from the subsequent VI-based modeling, and the remaining nine VIs are retained as input variables.

4.2 Band sensitivity and GLCM strategy analysis

To evaluate the effects of spectral bands and GLCM parameter settings on peanut AGB estimation, six regression models are applied to 36 TFs derived from each of the four multispectral bands, with R^2 and RMSE used as evaluation metrics. As shown in Fig. 4, the NIR band generally produces the lowest RMSE values, while Fig. 5 shows that it achieves the highest R^2 values across most models. The red-edge band shows intermediate performance and generally outperforms the green band (Fig. 4), whereas the red band produces the poorest results, including negative R^2 values in several models, such as DTR, RFR, MLR, and PLSR (Fig. 5).

The superior performance of the NIR-derived TFs may be attributed to the sensitivity of NIR reflectance to the leaf internal structure, canopy spatial heterogeneity, and moisture-related variation. These characteristics enable the NIR textures to capture biomass-related structural information while showing lower saturation than the visible bands. In contrast, strong chlorophyll absorption and spectral saturation under dense canopy conditions reduce the sensitivity of the red-band textures to AGB variation. Therefore, the NIR band is selected for the subsequent optimization of GLCM parameters and peanut AGB modeling.

The window size, orientation, and gray-level quantization of the GLCM jointly determine the spatial scale, directional sensitivity, and information granularity of texture representation. Their combined effects are therefore evaluated rather than considering each parameter independently.

Window size determines the spatial extent over which local texture statistics are calculated. A small window, such as 3×3, may capture fine-scale pixel variation but may be insufficient to represent integrated peanut canopy structures. In contrast, a larger window can incorporate more complete canopy information, although an excessively large window may smooth local variation. As shown in Table S3 in the supplementary materials, the high-performing configurations are mainly concentrated at window sizes of 5×5 and 7×7, whereas the 3×3 window appears only in a limited number of top-performing combinations. Because biomass variation during the middle and late growth stages is primarily reflected by canopy-scale structural changes, the 7×7 window is considered more suitable for representing AGB-related texture patterns.

The directional parameter reflects the orientation-dependent arrangement of canopy textures. Although averaging GLCM features across multiple directions can reduce directional variability, it may also introduce redundant information and weaken orientation-specific responses. The 45° direction occurs most frequently among the high-performing parameter combinations, whereas the 135° direction appears less frequently (Table S3 in the supplementary materials). Peanut is planted in rows, and its canopy expands both along and across the planting direction during biomass accumulation. Therefore, the 45° orientation may better integrate these two spatial components and capture irregular canopy texture patterns while reducing the dominance of row spacing that may occur at 0° or 90°.

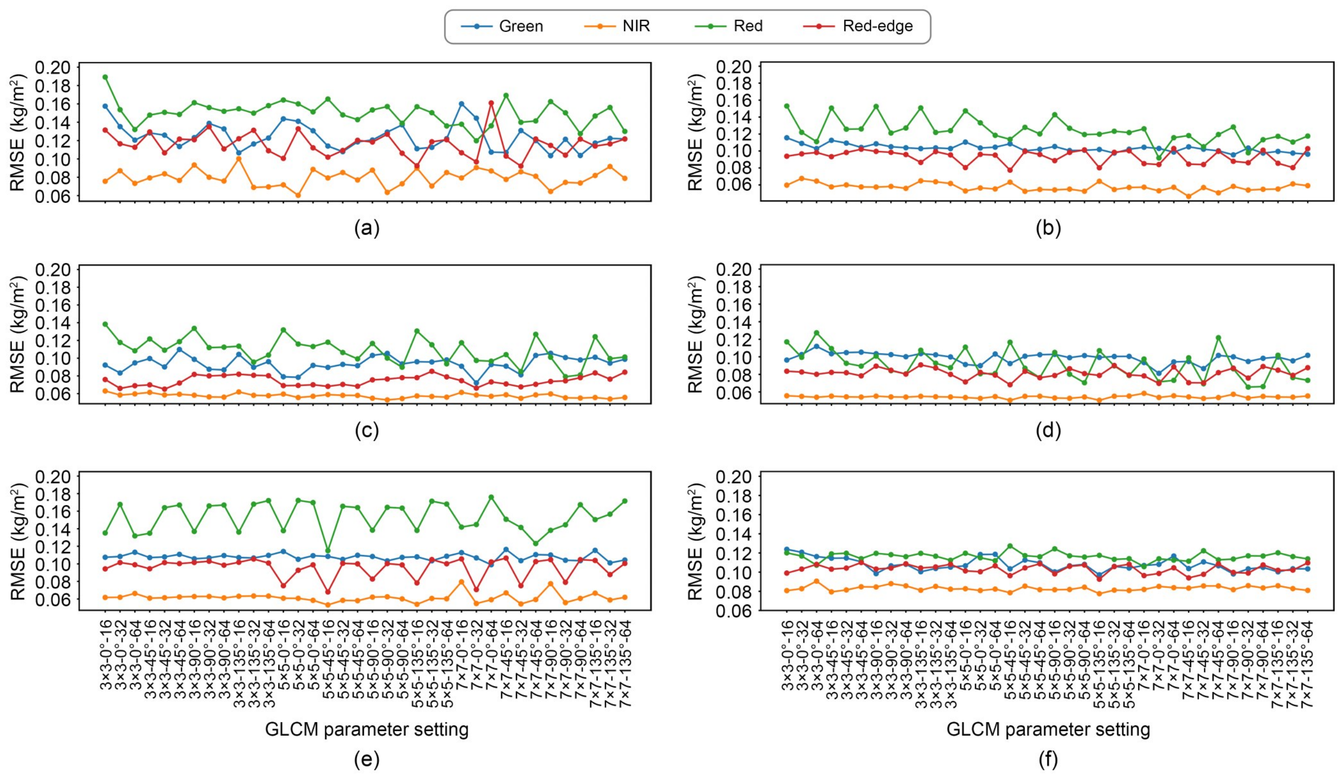

Fig. 4 RMSE of the observed versus predicted biomass values based on 36 GLCM TFs: (a) DTR model; (b) RFR model; (c) MLR model; (d) RR model; (e) PLSR model; (f) SVR model

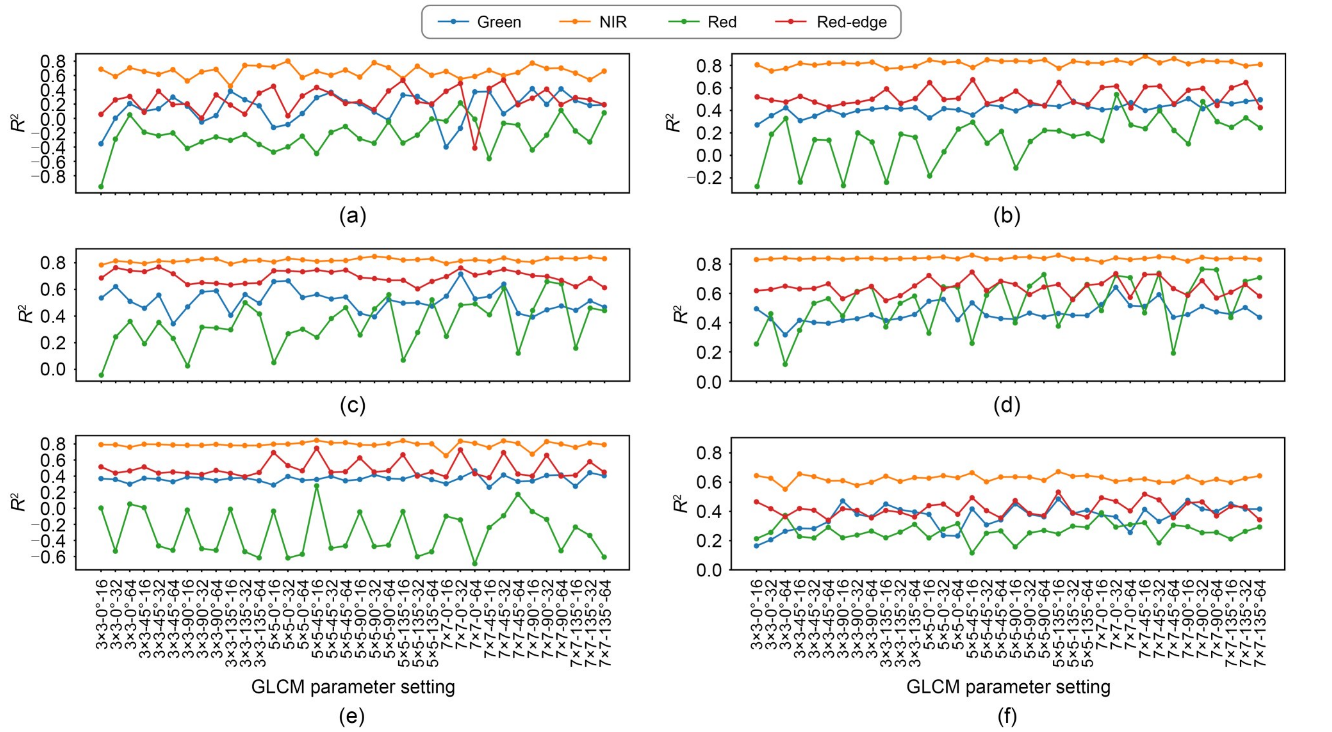

Fig. 5 R^2 of the observed versus predicted biomass values based on 36 GLCM TFs: (a) DTR model; (b) RFR model; (c) MLR model; (d) RR model; (e) PLSR model; (f) SVR model

Gray-level quantization affects the balance between texture-detail preservation and noise suppression. The configurations with 16 or 32 gray levels generally achieve better performance than those with 64 gray levels, although 64 levels produce competitive results in a few cases, such as RFR and DTR (Table S3 in the supplementary materials). A larger gray-level number preserves finer gray-scale variation but may disperse the dominant canopy contrasts into numerous bins and increase sensitivity to image noise. In comparison, 16-level quantization retains the principal structural differences associated with biomass while reducing redundant gray-scale information.

Overall, although the model-specific optimal combinations vary, the NIR-derived GLCM textures calculated using a 7×7 window size, a 45° orientation, and 16 gray levels provide the most stable and interpretable representation of peanut canopy structure across the evaluated models. This configuration is therefore adopted for subsequent peanut AGB estimation.

4.3 Peanut AGB estimation models based on different features

To evaluate the effects of different feature types on peanut AGB estimation, three feature configurations—the remaining nine VIs, eight TFs, and their combination—are used to construct six regression models. The performance of these models is compared based on R^2, adjusted R^2, and RMSE.

For the VIs-based models (Table 4), linear regression models generally show better performance than nonlinear models. Among the evaluated models, RR achieves the best prediction accuracy, with R^2 of 0.896, adjusted R^2 of 0.874, and RMSE of 0.044 kg/m^2 (Table 4). In contrast, DTR shows the poorest performance (R^2=0.547, adjusted R^2=0.450, and RMSE=0.091 kg/m^2), suggesting limited stability when using VIs as input variables. Overall, the results indicate that VIs provide effective spectral information for AGB estimation, with linear models showing stronger predictive capability under the current feature conditions.

Table 4 Performance of regression models using VIs and TFs

Model	VIs-based			TFs-based		
	Adjusted R^2	R^2	RMSE (kg/m^2)	Adjusted R^2	R^2	RMSE (kg/m^2)
DTR	0.450	0.547	0.091	0.745	0.785	0.063
SVR	0.811	0.845	0.053	0.653	0.708	0.073
RFR	0.809	0.843	0.054	0.836	0.862	0.050
RR	0.874	0.896	0.044	0.804	0.834	0.055
PLSR	0.861	0.886	0.046	0.802	0.833	0.055
MLR	0.855	0.881	0.047	0.834	0.860	0.051

For the TFs-based models (Table 4), the optimal GLCM configuration (a 7×7 window size, a 45° orientation, and 16 gray levels) is used to generate texture variables. Among the six models, RFR achieves the best performance among nonlinear methods, with an adjusted R^2 of 0.836 and RMSE of 0.050 kg/m^2. Among linear models, MLR shows comparable performance, achieving an adjusted R^2 of 0.834 and RMSE of 0.051 kg/m^2. Although SVR and DTR show relatively lower accuracy, the overall results demonstrate that TFs provide complementary structural information for peanut AGB estimation.

When combining VIs and TFs (Fig. 6), the prediction performance improves for most regression models. Among all evaluated models, PLSR achieves the best performance, with R^2 of 0.919, adjusted R^2 of 0.879, and RMSE of 0.038 kg/m^2 (Fig. 6b). RR ranks second (Fig. 6d), whereas MLR shows relatively limited improvement,

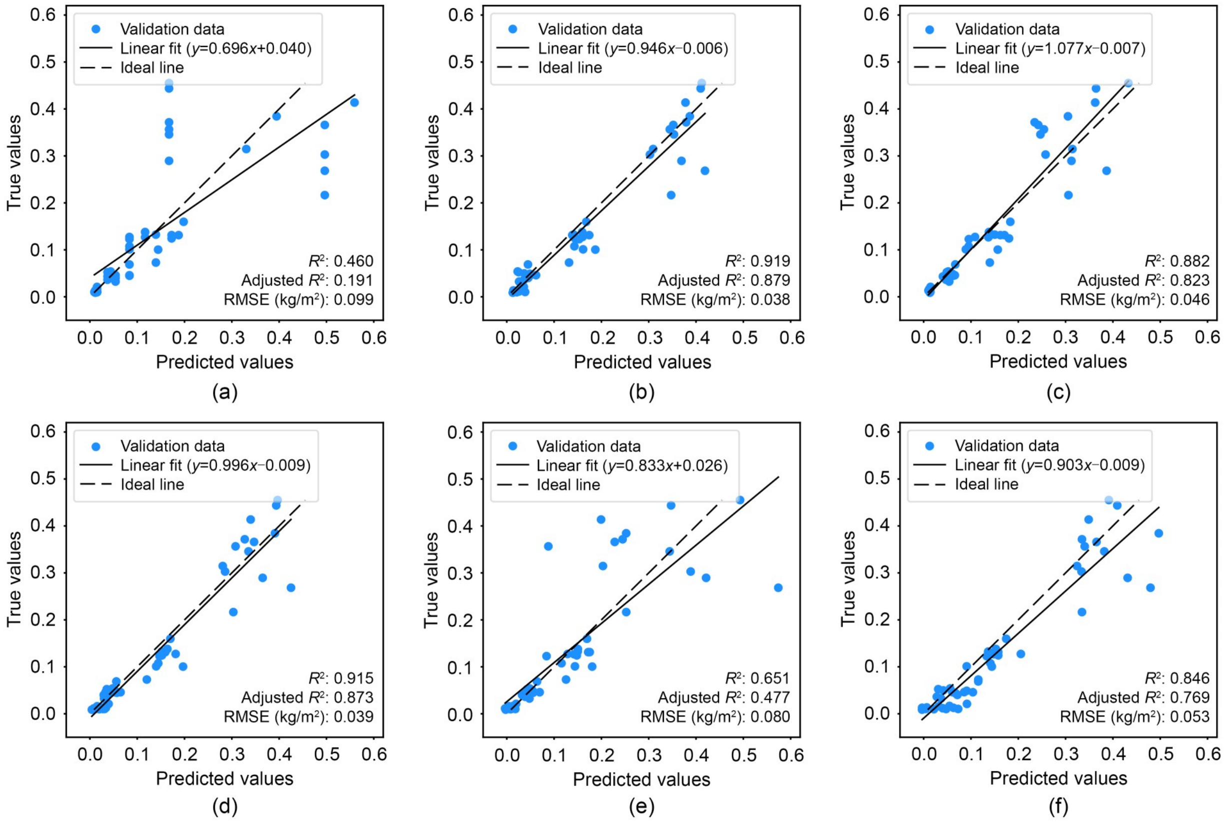

Fig. 6 Predicted versus observed peanut biomass values based on the combination of VI and TF: (a) DTR model; (b) PLSR model; (c) RFR model; (d) RR model; (e) SVR model; (f) MLR model

possibly because of its sensitivity to redundant variables (Fig. 6f). Among the nonlinear models, RFR maintains the best performance (Fig. 6c), while DTR and SVR produce relatively unstable predictions (Figs. 6a and 6e).

Although integrating spectral and textural features generally improves the prediction accuracy, the adjusted R^2 values of some models remain substantially lower than their corresponding R^2 values. In particular, the differences reach 0.174 for SVR and 0.077 for MLR (Figs. 6e and 6f, respectively). These gaps indicate that the apparent increases in R^2 are accompanied by a larger penalty after accounting for predictor number, suggesting that some variables in the combined feature set provide limited incremental explanatory value. The results therefore indicate reduced model parsimony and potential predictor redundancy, motivating the subsequent feature-selection analysis.

5 Discussion

5.1 Comparison of feature selection strategies

As shown in Section 4.3, combining the nine VIs and eight TFs increases the number of input variables to 17, whereas the improvement in model performance is relatively limited. Therefore, Boruta and XGBoost-SHAP are compared to evaluate the effectiveness of feature selection and identify a compact feature representation for peanut AGB estimation.

Boruta retains 14 relevant variables, including nine VIs (DVI, GNDVI, MSAVI, NDRE, NDVI, NIRv, OSAVI, RVI, and SAVI) and five TFs (contrast, energy, homogeneity, mean, and variance). In comparison, the five highest-ranked features according to their mean absolute SHAP values are DVI, MSAVI, mean, variance, and energy, which constitute the XGBoost-SHAP selected-feature subset (Fig. S3 in the supplementary materials). Regression models are subsequently constructed using the two feature subsets, and their performance is summarized in Table 5.

Table 5 Comparison of the model performance using Boruta and XGBoost-SHAP selected-feature sets

Model	Boruta (14 variables)			XGBoost-SHAP (five variables)		
	Adjusted R^2	R^2	RMSE (kg/m^2)	Adjusted R^2	R^2	RMSE (kg/m^2)
DTR	0.255	0.460	0.100	0.830	0.847	0.053
SVR	0.718	0.811	0.072	0.839	0.855	0.052
RFR	0.836	0.881	0.047	0.857	0.871	0.049
RR	0.884	0.916	0.039	0.878	0.890	0.045
PLSR	0.890	0.920	0.038	0.865	0.878	0.047
MLR	0.844	0.887	0.046	0.865	0.878	0.047

Both feature selection methods retain variables that support accurate peanut AGB estimation. The Boruta selected-feature subset achieves the lowest RMSE with PLSR (0.038 kg/m^2), but its performance varies more markedly among models, with RMSE of DTR reaching 0.100 kg/m^2. The XGBoost-SHAP selected-feature subset produces RMSE values of 0.045–0.053 kg/m^2 across the six models, while the differences between R^2 and adjusted R^2 remain below

0.020, indicating only a small penalty after accounting for predictor number.

The differences between the selected subsets are consistent with the principles of the two methods. Boruta follows an all-relevant strategy and may retain correlated variables that consistently outperform randomized shadow features (Kursa and Rudnicki, 2010), whereas, in the XGBoost-SHAP approach, SHAP values quantify the contribution of individual variables to the predictions of the XGBoost model (Lundberg and Lee, 2017). The comparison does not indicate that either method is universally superior; rather, the five-variable subset identified by XGBoost-SHAP is adopted because it better matches the objective of reducing feature dimensionality and redundancy while maintaining consistent predictive performance.

5.2 Algorithm repeatability under different feature configurations

Building on the feature selection results in Section 5.1, the robustness of the three feature configurations to data partitioning is further evaluated using 50 repeated random plot-level training–validation splits. In each repetition, 30 plots are randomly assigned to the training set and the remaining 13 plots are used for validation, while the observations from all four growth stages for each plot are retained in the same subset. The three input configurations are the nine-VI feature set, the eight-TF feature set, and the XGBoost-SHAP selected-five-feature set consisting of DVI, MSAVI, mean, variance, and energy. Model hyperparameters remain unchanged across repetitions. The distributions of validation adjusted R^2 and RMSE are used to evaluate the sensitivity of the models to different data partitions and to compare the predictive robustness of the three feature configurations.

As shown in Fig. S4 in the supplementary materials, the five-feature set generally produces higher median adjusted R^2 values and lower median RMSE values than the VI and TF feature sets across the evaluated models. Its interquartile ranges are also generally narrower, indicating lower sensitivity to variations in the training and validation samples and more consistent predictive performance across different random plot-level partitions.

These results indicate that combining DVI and MSAVI with mean, variance, and energy preserves complementary spectral and structural information while reducing feature dimensionality. The five-feature representation therefore provides a favorable balance between predictive accuracy, feature compactness, and robustness to changes in data partitioning under the current experimental conditions.

5.3 Biophysical interpretation of the selected features

The effectiveness of the five-feature subset (DVI, MSAVI, mean, variance, and energy) can be attributed to its ability to represent two major processes associated with peanut biomass accumulation: the increase in photosynthetically active tissues and the spatial reorganization of the low-growing and laterally expanding canopy. DVI and MSAVI characterize changes in canopy spectral response, whereas the NIR-derived TFs describe variations in canopy coverage and structural heterogeneity.

DVI and MSAVI are particularly relevant to peanut growth because the contribution of the soil background changes substantially during canopy development. At the seedling and flowering–pod initiation stages, the peanut canopy occupies only part of the ridge surface, and exposes soil between plants and rows; the exposed soil contributes noticeably to the plot-level spectral response. MSAVI reduces this background influence and is therefore useful for characterizing early canopy development. As peanut branches and leaves expand laterally during the subsequent growth stages, the proportion of photosynthetically active vegetation increases, strengthening red-band absorption and NIR reflectance and enhancing the response of DVI to biomass accumulation (Tan et al., 2025). However, as neighboring plants overlap and the canopy gradually closes, spectral indices become increasingly susceptible to saturation, limiting their sensitivity to further increases in AGB (Yue et al., 2023).

The NIR-derived mean, variance, and energy provide complementary information on the distinctive structural development of the peanut canopy. NIR reflectance is strongly influenced by the internal leaf structure and multiple scattering within the canopy rather than solely by pigment concentration (Zhang SH et al., 2024). Mean represents the average gray-level response within each plot and reflects changes in the relative proportions of vegetation and exposed background. Variance characterizes spatial heterogeneity arising from leaves, shadows, canopy gaps, and inter-row background, whereas energy describes the regularity of the gray-level distribution. As peanut plants expand horizontally and adjacent canopies begin to overlap, these texture metrics capture the transition from spatially separated plants to a denser and more continuous canopy surface (Freitas et al., 2022; Xu TY et al., 2022).

The GLCM configuration identified in Section 4.2 ensures that these structural features are extracted at a spatial scale suitable for the double-row planting pattern and lateral canopy expansion of peanut, consistent with the scale dependence of texture analysis. Overall, DVI and MSAVI represent changes in green vegetation and soil-background influence, while mean, variance, and energy capture canopy coverage, gap distribution, and structural organization. Their combination therefore provides complementary physiological and structural information specifically relevant to peanut AGB estimation.

5.4 Interpretation of the favorable performance of linear models

As shown by the preceding results, linear models generally achieve higher or comparable estimation accuracy when VIs or the optimized lightweight feature set is used as input. This performance may be attributed to the high informativeness of the engineered predictors. Rather than using raw spectral bands or pixel gray values directly, the models use VIs and GLCM-derived texture metrics that have already summarized the principal physiological and structural information associated with peanut biomass. After redundant variables are reduced through feature selection, the relationships between the selected predictors and AGB can be adequately represented by relatively simple linear models within the biomass range investigated in this study. Consequently, the additional flexibility of nonlinear algorithms does not consistently produce further performance gains.

Nevertheless, RFR slightly outperforms the other models when TFs alone are used, indicating that nonlinear response patterns may still exist within canopy structural descriptors. Therefore, the favorable performance of linear models is mainly observed for VI-based and optimized lightweight inputs rather than across all feature configurations. These findings suggest that model performance depends on the compatibility between feature representation and the underlying feature–AGB relationships, rather than on model complexity alone.

5.5 Limitations and future research directions

The structural interpretation of the NIR-derived TFs is inferred from image-based spectral–structural relationships rather than directly verified using field measurements of canopy architecture. Future studies should incorporate measurements such as canopy cover, plant height, leaf area index, and three-dimensional canopy structure to validate the physical meanings of the selected TFs. Hyperspectral or light detection and ranging (LiDAR) observations may also be used as complementary reference data for mechanistic validation, while the multispectral-based lightweight framework remains the primary approach for practical high-throughput peanut AGB monitoring.

6 Conclusions

This study develops a UAV multispectral imagery-based framework for high-throughput estimation of peanut aboveground biomass. NIR-derived TFs show the strongest sensitivity to AGB, and the optimal GLCM configuration is a 7×7 window size, a 45° orientation, and 16 gray levels. XGBoost-SHAP identifies five key features—DVI, MSAVI, mean, variance, and energy—which substantially reduce feature redundancy while maintaining stable prediction performance (R^2>0.840, adjusted R^2≥0.830, RMSE<0.055 kg/m^2, and the differences between R^2 and adjusted R^2<0.020). The resulting lightweight spectral–textural feature set provides a practical approach for high-throughput peanut phenotyping and field-scale biomass monitoring.

Supplementary information

The online version contains supplementary materials available at https://doi.org/10.1631/ENG.ITEE.2026.0108.

Acknowledgments

This work was supported by the Key R&D Program of Shandong Province, China (No. 2022LZGC021), the Guangxi Science and Technology Program (No. GKFN2600640051), and the Youth Innovation Science and Technology Support Program for Institutions of Higher Education in Shandong Province (No. 2024KJH062).

Author contributions

Liya HU drafted the paper and performed the experiments. Bo BAI contributed to the organization of the paper and performed the experiments. Mingxuan SONG, Youwei LI, Dandan LIU, and Zhenhai LI assisted with the data processing. Yirou LIU contributed to the methodology and resources. Juntao YANG designed the study and supervised the research. Guowei LI provided funding support and supervised the project. All the authors reviewed and approved the final paper.

Conflict of interest

All the authors declare that they have no conflict of interest.

Data availability

The data that support the findings of this study are available from the corresponding authors upon reasonable request.

Declaration on the use of generative AI tools

During the preparation of this work, the authors used ChatGPT and AJE to improve language. After using these tools, the authors reviewed and edited the content as needed and take full responsibility for the content of the published article.

References

Balling J, Herold M, Reiche J, 2023. How textural features can improve SAR-based tropical forest disturbance mapping. *Int J Appl Earth Obs Geoinf*, 124:103492. https://doi.org/10.1016/j.jag.2023.103492

Bodoira R, Cittadini MC, Velez A, et al., 2022. An overview on extraction, composition, bioactivity and food applications of peanut phenolics. *Food Chem*, 381:132250. https://doi.org/10.1016/j.foodchem.2022.132250

Burnett AC, Anderson J, Davidson KJ, et al., 2021. A best-practice guide to predicting plant traits from leaf-level hyperspectral data using partial least squares regression. *J Exp Bot*, 72(18):6175-6189. https://doi.org/10.1093/jxb/erab295

Burns BW, Green VS, Hashem AA, et al., 2022. Determining nitrogen deficiencies for maize using various remote sensing indices. *Precision Agric*, 23(3):791-811. https://doi.org/10.1007/s11119-021-09861-4

Cen HY, Wan L, Zhu JP, et al., 2019. Dynamic monitoring of biomass of rice under different nitrogen treatments using a lightweight UAV with dual image-frame snapshot cameras. *Plant Methods*, 15(1):32. https://doi.org/10.1186/s13007-019-0418-8

Chen H, Li W, Zhu YY, 2021. Improved window adaptive gray level co-occurrence matrix for extraction and analysis of texture characteristics of pulmonary nodules. *Comput Methods Programs Biomed*, 208:106263. https://doi.org/10.1016/j.cmpb.2021.106263

Fan YG, Feng HK, Yue JB, et al., 2023. Using an optimized texture index to monitor the nitrogen content of potato plants over multiple growth stages. *Comput Electr Agric*, 212:108147. https://doi.org/10.1016/j.compag.2023.108147

Franceschini MHD, Becker R, Wichern F, et al., 2022. Quantification of grassland biomass and nitrogen content through UAV hyperspectral imagery—active sample selection for model transfer. *Drones*, 6(3):73. https://doi.org/10.3390/drones6030073

Freitas RG, Pereira FRS, Dos Reis AA, et al., 2022. Estimating pasture aboveground biomass under an integrated crop-livestock system based on spectral and texture measures derived from UAV images. *Comput Electr Agric*, 198:107122. https://doi.org/10.1016/j.compag.2022.107122

He LM, Wang R, Mostovoy G, et al., 2021. Crop biomass mapping based on ecosystem modeling at regional scale using high resolution Sentinel-2 data. *Remote Sens*, 13(4): 806. https://doi.org/10.3390/rs13040806

Hosseini Taheri SE, Bazargan M, Rahnama Vosough P, et al., 2024. A comprehensive insight into peanut: chemical structure of compositions, oxidation process, and storage conditions. *J Food Compost Anal*, 125:105770. https://doi.org/10.1016/j.jfca.2023.105770

Hou XH, Zhang JY, Luo XB, et al., 2025. Peanut yield prediction using remote sensing and machine learning approaches based on phenological characteristics. *Comput Electr Agric*, 232:110084. https://doi.org/10.1016/j.compag.2025.110084

Kayad A, Rodrigues FA, Naranjo S, et al., 2022. Radiative transfer model inversion using high-resolution hyperspectral airborne imagery–retrieving maize LAI to access biomass and grain yield. *Field Crops Res*, 282:108449. https://doi.org/10.1016/j.fcr.2022.108449

Kursa MB, Rudnicki WR, 2010. Feature selection with the Boruta package. *J Stat Softw*, 36(11):1-13. https://doi.org/10.18637/jss.v036.i11

Li S, Potter C, 2012. Patterns of aboveground biomass regeneration in post-fire coastal scrub communities. *GISci Remote Sens*, 49(2):182-201. https://doi.org/10.2747/1548-1603.49.2.182

Liang YY, Kou WL, Lai HY, et al., 2022. Improved estimation of aboveground biomass in rubber plantations by fusing spectral and textural information from UAV-based RGB imagery. *Ecol Ind*, 142:109286. https://doi.org/10.1016/j.ecolind.2022.109286

Liu Y, Feng HK, Fan YG, et al., 2024a. Improving potato above ground biomass estimation combining hyperspectral data and harmonic decomposition techniques. *Comput Electr Agric*, 218:108699. https://doi.org/10.1016/j.compag.2024.108699

Liu Y, Fan YG, Feng HK, et al., 2024b. Estimating potato above-ground biomass based on vegetation indices and texture features constructed from sensitive bands of UAV hyperspectral imagery. *Comput Electr Agric*, 220:108918. https://doi.org/10.1016/j.compag.2024.108918

Lundberg SM, Lee SI, 2017. A unified approach to interpreting model predictions. Proc 31st Int Conf on Neural Information Processing Systems, p.4768-4777.

Niu YX, Song XY, Zhang LX, et al., 2025. Enhancing model accuracy of UAV-based biomass estimation by evaluating effects of image resolution and texture feature extraction strategy. *IEEE J Sel Top Appl Earth Obs Remote Sens*, 18:878-891. https://doi.org/10.1109/JSTARS.2024.3501673

Nohara Y, Matsumoto K, Soejima H, et al., 2022. Explanation of machine learning models using Shapley additive explanation and application for real data in hospital.

Comput Methods Programs Biomed, 214:106584. https://doi.org/10.1016/j.cmpb.2021.106584

Qiao L, Tang WJ, Gao DH, et al., 2022. UAV-based chlorophyll content estimation by evaluating vegetation index responses under different crop coverages. *Comput Electr Agric*, 196:106775. https://doi.org/10.1016/j.compag.2022.106775

Schober P, Boer C, Schwarte LA, 2018. Correlation coefficients: appropriate use and interpretation. *Anesth Analg*, 126(5):1763-1768. https://doi.org/10.1213/ane.0000000000002864

Shu MY, Li Q, Ghafoor A, et al., 2023. Using the plant height and canopy coverage to estimation maize aboveground biomass with UAV digital images. *Eur J Agron*, 151: 126957. https://doi.org/10.1016/j.eja.2023.126957

Song MX, Bai B, Yang JT, et al., 2025. Robust UAV-based method for peanut plant height estimation using bare-soil invariant constraints. *Smart Agric*, 7(6):124-135 (in Chinese). https://doi.org/10.12133/j.smartag.SA202509029

Tan HJ, Kou WL, Xu WH, et al., 2025. Enhancing aboveground biomass estimation in rubber plantations using UAV multispectral data for satellite upscaling. *Remote Sens*, 17(17):2955. https://doi.org/10.3390/rs17172955

Wang F, Yang M, Ma LF, et al., 2022. Estimation of above-ground biomass of winter wheat based on consumer-grade multi-spectral UAV. *Remote Sens*, 14(5):1251. https://doi.org/10.3390/rs14051251

Wang S, Guan KY, Wang ZH, et al., 2021. Airborne hyperspectral imaging of nitrogen deficiency on crop traits and yield of maize by machine learning and radiative transfer modeling. *Int J Appl Earth Obs Geoinf*, 105:102617. https://doi.org/10.1016/j.jag.2021.102617

Xu L, Zhou LF, Meng R, et al., 2022. An improved approach to estimate ratoon rice aboveground biomass by integrating UAV-based spectral, textural and structural features. *Precision Agric*, 23(4):1276-1301. https://doi.org/10.1007/s11119-022-09884-5

Xu TY, Wang FM, Xie LL, et al., 2022. Integrating the textural and spectral information of UAV hyperspectral images for the improved estimation of rice aboveground biomass. *Remote Sens*, 14(11):2534. https://doi.org/10.3390/rs14112534

Yang N, Zhang ZT, Zhang JR, et al., 2023. Improving estimation of maize leaf area index by combining of UAV-based multispectral and thermal infrared data: the potential of new texture index. *Comput Electr Agric*, 214:108294. https://doi.org/10.1016/j.compag.2023.108294

Yu FH, Bai JC, Fang JY, et al., 2024. Integration of a parameter combination discriminator improves the accuracy of chlorophyll inversion from spectral imaging of rice. *Agric Commun*, 2(3):100055. https://doi.org/10.1016/j.agrcom.2024.100055

Yue JB, Yang H, Yang GJ, et al., 2023. Estimating vertically growing crop above-ground biomass based on UAV remote sensing. *Comput Electr Agric*, 205:107627. https://doi.org/10.1016/j.compag.2023.107627

Zhang JY, Qiu XL, Wu YT, et al., 2021. Combining texture, color, and vegetation indices from fixed-wing UAS imagery to estimate wheat growth parameters using multivariate regression methods. *Comput Electr Agric*, 185:106138. https://doi.org/10.1016/j.compag.2021.106138

Zhang SH, Duan JZ, Qi XH, et al., 2024. Combining spectrum, thermal, and texture features using machine learning algorithms for wheat nitrogen nutrient index estimation and model transferability analysis. *Comput Electr Agric*, 222:109022. https://doi.org/10.1016/j.compag.2024.109022

Zhang Y, Xia CZ, Zhang XY, et al., 2021. Estimating the maize biomass by crop height and narrowband vegetation indices derived from UAV-based hyperspectral images. *Ecol Ind*, 129:107985. https://doi.org/10.1016/j.ecolind.2021.107985

Zheng HB, Cheng T, Li D, et al., 2018. Combining unmanned aerial vehicle (UAV)-based multispectral imagery and ground-based hyperspectral data for plant nitrogen concentration estimation in rice. *Front Plant Sci*, 9:936. https://doi.org/10.3389/fpls.2018.00936